HII region G46.5-0.2: the interplay between ionizing radiation, molecular gas and star formation

S. Paron[1,2], M. E. Ortega[1], G. Dubner [1], Jing-Hua Yuan [3], A. Petriella[1], E. Giacani[1,2], Jin Zeng Li[3], Yuefang Wu[4], Hongli Liu[3], Ya Fang Huang[3], and Si-Ju Zhang[3]

`sparon@iafe.uba.ar`

arXiv:1504.03935v1 [astro-ph.GA] 15 Apr 2015

[1]Instituto de Astronomía y Física del Espacio (IAFE, CONICET-UBA), CC 67, Suc. 28, 1428 Buenos Aires, Argentina

[2]FADU - Universidad de Buenos Aires, Ciudad Universitaria, Buenos Aires, Argentina

[3]National Astronomical Observatories, Chinese Academy of Sciences, 20A Datun Road, Chaoyang District, Beijing 100012, China

[4]Department of Astronomy, Peking University, 100871 Beijing, China

ABSTRACT

Hii regions are particularly interesting because they can generate dense layers of gas and dust, elongated columns or pillars of gas pointing towards the ionizing sources, and cometary globules of dense gas, where triggered star formation can occur. Understanding the interplay between the ionizing radiation and the dense surrounding gas is very important to explain the origin of these peculiar structures, and hence to characterize triggered star formation. G46.5-0.2 (G46), a poorly studied galactic HII region located at about 4 kpc, is an excellent target to perform this kind of studies. Using public molecular data extracted from the Galactic Ring Survey (^{13}CO J=1–0) and from the James Clerk Maxwell Telescope data archive (^{12}CO, ^{13}CO, C^{18}O J=3–2, HCO$^+$ and HCN J=4–3), and infrared data from the GLIMPSE and MIPSGAL surveys, we perform a complete study of G46, its molecular environment and the young stellar objects placed around it. We found that G46, probably excited by an O7V star, is located close to the edge of the GRSMC G046.34-00.21 molecular cloud. It presents a horse-shoe morphology opening in direction of the cloud. We observed a filamentary structure in the molecular gas likely related to G46 and not considerable molecular emission towards its open border. We found that about 10′ towards the southwest of G46 there are some pillar-like features, shining at 8 μm and pointing towards the Hii region open border. We propose that the pillar-like features were carved and sculpted by the ionizing flux from G46. We found several young stellar objects likely embedded in the molecular cloud grouped in two main concentrations: one, closer to the G46 open border consisting of Class II type sources, and other one mostly composed by Class I type YSOs located just ahead the pillars-like features, strongly suggesting an age gradient in the YSOs distribution.

Subject headings: ISM: Hɪɪ regions – individual: G46.5-0.2 – ISM: molecular clouds – individual: GRSMC G046.34-00.21 – Stars: formation – ISM: molecules

1. Introduction

Massive stars play a key role in the evolution of the Galaxy. They are the principal source of heavy elements and UV radiation. Through the combination of winds, massive outflows, expanding HII regions and supernova explosions, they provide an important source of mixing turbulence in the interstellar medium (ISM). HII regions are particularly interesting because they can trigger the formation of a new generation of stars. Processes such 'collect and collapse' (e.g. Elmegreen et al. 1995) and radiative driven implosion (RDI) (e.g. Bertoldi 1989) have been convincingly demonstrated that occur around HII regions leading to formation of stars (e.g. Ortega et al. 2013; Dirienzo et al. 2012; Paron et al. 2011; Zavagno et al. 2010; Deharveng et al. 2008; Thompson et al. 2004a). These processes generate dense layers of gas and dust at the interface between the HII regions and their parent molecular cloud, elongated columns (pillars) of gas pointing towards the ionizing sources, and cometary globules of dense gas (Tremblin et al. 2013). Understanding the interplay between the ionizing radiation and the dense surrounding gas is very important to explain the origin of these peculiar structures, and hence to characterize triggered star formation.

G46.5-0.2 (hereafter G46) is a poorly studied HII region about $8'$ in size located at RA $= 19^{\mathrm{h}}17^{\mathrm{m}}26ß$, dec $= 11°55'54''$ (J2000), on the border of the molecular cloud catalogued as GRSMC G046.34-00.21 (Rathborne et al. 2009). Lockman (1989) observed a recombination line at $v_{\mathrm{LSR}} \sim 57.2$ km s^{-1} towards this region. Kuchar & Bania (1994) detected HI absorption features up to 56.6 km s^{-1} and based on kinematical considerations proposed for this HII region the near distance of 3.8 kpc, while Quireza et al. (2006), using the same techniques, favored the far distance of 7.8 kpc. Finally, Anderson & Bania (2009) resolved the kinematic distance ambiguity for G46 based on existing HI and ^{13}CO sky surveys, confirming a near distance of 4 kpc, which will be adopted in what follows.

Figure 1 shows a two-color composite image of G46 field where the *Spitzer*-IRAC 8 μm emission distribution is displayed in cyan and the *Spitzer*-MIPSGAL at 24 μm in red. The emission displayed in cyan mainly corresponds to radiation originated in polycyclic aromatic hydrocarbon (PAH) molecules. The far-UV photons leaking from the HII region excite the PAHs, which then emit in the mid-infrared. This emission encircles the 24 μm emission (in red) that arises from very small size dust grains which are heated but not destroyed by the UV photons. The emission at 8 μm has a horse-shoe morphology, being thicker and more intense towards the east-northeast direction and open to the southwest, where it dilutes into the surrounding medium. Precisely in the southwest direction, about 10$'$ away from G46 there are pillar-like features shining at 8 μm. In this paper we explore the interrelationship among the HII region G46, the environmental conditions and the young stellar objects in the region, underscoring evidence of triggered stellar formation in the immediate vicinity of G46 and farther.

2. Data

2.1. Molecular data

The ^{13}CO J=1–0 data were extracted from the Galactic Ring Survey (GRS). The survey, performed by the Boston University and the Five College Radio Astronomy Observatory, maps the Galactic Ring in the mentioned molecular line with an angular and spectral resolutions of 46$''$ and 0.2 km s^{-1}, respectively (see Jackson et al. 2006). The observations were performed in both position-switching and on-the-fly mapping modes, achieving an angular sampling of 22$''$. Data are presented in main beam temperature (T_{mb}).

Additionally we used ^{12}CO, ^{13}CO, C^{18}O J=3–2, and HCO$^+$, HCN J=4–3 data extracted

from the James Clerk Maxwell Telescope (JCMT) data archive[1]. These observations (Proposal I.D M10AH02, P.I. Jonathan Williams) were carried out with the JCMT in Mauna Kea, Hawaii, using the HARP-ACSIS instrument. The angular and spectral resolutions are about $15''$ and 0.05 km s^{-1}. We used the reduced data (cal. level 2), which were reduced using the standard ORAC-DR pipelines[2]. Data are presented in units of corrected antenna temperature T_A^*, which is related to the main beam temperature (T_{mb}) using $T_{mb} = T_A^*/\eta_{mb}$. Following Buckle et al. (2009) a value of $\eta_{mb} = 0.6$ was used. The zenith opacity was between 0.04 and 0.06 for all the observed lines. Even though we extracted reduced data, in the case of C^{18}O J=3–2, HCO$^+$, and HCN J=4–3 data we applied a Hanning smoothing to improve the signal-to-noise ratio which altered the spectral resolution in no more than a factor of 2, and minor polynomials were used for baseline corrections using XSpec[3].

2.2. Infrared data

In this work, archived infrared data are also used to reveal star formation in G46. These data come from the GLIMPSE and MIPSGAL surveys.

GLIMPSE (Galactic Legacy Infared Mid-Plane Survey Extraodinaire, Benjamin et al. 2003) using the IRAC (using the InfraRed Array Camera, Fazio et al. 2004) on board the *Spitzer Space Telescope* (Werner et al. 2004) surveyed the inner 130 degrees of the Galactic Plane at 3.6, 4.5, 5.8, and 8.0 μm bands. The 5 σ sensitivities of the four bands are 0.2, 0.2,

---

[1]www.jach.hawaii.edu/JCMT/archive/

[2]http://www.jach.hawaii.edu/JCMT/archive/CADC_quickguide.html

[3]XSpec is a spectral line reduction package for astronomy which has been developed by Per Bergman at Onsala Space Observatory.

0.4, 0.4 mJy, respectively. In addition to images, GLIMPSE survey performed point-source photometry. Photometric data at the J (1.25 μm), H (1.65 μm), and Ks (2.17 μm) bands from the Two Micron All Sky Point Source Catalog (2MASS PSC, Skrutskie et al. 2006) are provided in the GLIMPSE Catalog to build-up a 7-bands photometric system. Both the images and the catalog of GLIMPSE are publicly available at the InfraRed Science Archive (IRSA)[4], where we have retrieved cutouts in the four IRAC bands and point sources in a $31' \times 24'$ region centered at $\alpha_{2000} = 19^{\mathrm{h}}17^{\mathrm{m}}18^{\mathrm{s}}.7$, $\delta_{2000} = +11°52'22''.9$. We restricted the extracted catalog to be a more reliable data set with the following criteria: a) only sources with photometric errors no larger than 0.2 mag in the IRAC bands are taken into account; b) for 2MASS bands, a threshold of 0.1 mag photometric error is used to forsake unreliable photometric values. The photometric errors for IRAC and 2MASS sources have been adopted following Gutermuth et al. (2009).

MIPSGAL (Carey et al. 2009) is a complement to the GLIMPSE legacy survey. This survey using the MIPS (Multiband Infrared Photometer for *Spitzer*, Rieke et al. 2004) instrument on board the *Spitzer Space Telescope* surveyed an area comparable to that of GLIMPSE. The version 3.0 of MIPSGAL data includes mosaics only at 24 μm with sky coverage of $|b| < 1°$ for $-68° < l < 69°$, and $|b| < 3°$ for $-8° < l < 9°$. The spatial resolution and 5σ sensitivity at 24 μm are $6''$ and 1.7 mJy. From the IRSA server, we have extracted a cutout of a region same as that of GLIMPSE cutouts.

We conducted point-source extraction and aperture photometry of point sources in the MIPS 24 μm image using the PSF fitting capability of IRAF/DAOPHOT (Stetson 1987). The PSF was determined to be about $6''$ by fitting the profiles of ten bright point sources in the investigated field. The standard deviation (σ) of the sky was estimated to be about 5.0×10^{-6} Jy pixel^{-1}. DAOFIND was used to extract candidates of point sources

---

[4]http://irsa.ipac.caltech.edu/index.html

with a threshold of 10 σ. The final sources were determined by visual inspection using the TVMARK task. Sources affected by ghosts, diffraction spikes, halos from bright sources and artifacts residing in bright extended emission were rejected. For aperture photometry of the extracted sources, radii of the apertures and inner and outer limits of the sky annuli were selected to be 4.5″, 15″ and 21″, respectively. Magnitudes of the extracted sources were determined using the magnitude zero point of 7.17 Jy provided in the MIPS instrument handbook[5]. Finally, we cross-matched the 24 μm sources with the GLIMPSE catalog using a cone radius of 2″.

Additionally, we have queried the MIPSGAL point source catalog given by Gutermuth & Heyer (2015). A total of 309 sources are found in the region of interest. Among them, 305 have been covered by our 24 μm point source list. The other four sources are weaker than 11.5 mag. A comparison of the fluxes indicates that our photometry is consistent with that given in Gutermuth & Heyer (2015), the mean difference is smaller than 5% in magnitude.

The completeness of our catalog was estimated by counting the number of sources as a function of magnitude. A histogram plot of source magnitudes at each band has been plotted and carefully inspected. The sources magnitudes are exponentially distributed. We plot the number of sources in log scale and the magnitude in linear scale, then a straight line can be fitted. The magnitude at which a deviation emerges has been considered as the completeness limit. We found that our catalog is complete to a magnitude of 14.0 at 3.6 μm, 13.5 at 4.5 μm, 12.3 at 5.8 μm, 12.0 at 8.0 μm, and 8.5 at 24 μm. For the central region with diffuse mid-infrared emission, our catalog is complete to a magnitude of 14.0 at 3.6 μm, 13.5 at 4.5 μm, 12.0 at 5.8 μm, 11.5 at 8.0 μm, and 8.0 at 24 μm.

---

[5]http://irsa.ipac.caltech.edu/data/SPITZER/docs/mips/

3. Results and discussion

In what follows we separately analyze the physical properties of the HII region G46 (Sec. 3.1), of the ambient molecular gas (Sect. 3.2) and of the young stellar objects (YSOs) near G46 (Sec. 3.3), with the aim of investigating the impact of the ionizing radiation on the surrounding medium and the likelihood of triggered star formation.

3.1. Exciting star(s) candidate(s) and morphology of G46

A search for the exciting star of G46 in the available OB-type stars catalogues (Maíz Apellániz et al. 2013; Maíz-Apellániz et al. 2004; Reed 2003), was unsuccessful. We can, anyway, conjecture the earliest spectral type of a probable single ionizing star from the radio continuum emission of the HII region. The number of UV ionizing photons needed to keep an HII region ionized is given by $N_{\mathrm{UV}} = 0.76 \times 10^{47} T_4^{-0.45} \nu_{\mathrm{GHz}}^{0.1} S_\nu D_{\mathrm{kpc}}^2$ (Chaisson 1976), where T_4 is the electron temperature in units of 10^4 K, D_{kpc} the distance in kpc, ν_{GHz} the frequency in GHz, and S_ν the measured total flux density in Jy. Assuming a typical electron temperature of $T = 10^4$ K, a distance of 4 kpc, and a total flux density of 2.7 Jy as measured from the MAGPIS[6] image at 1.4 GHz, the total amount of ionizing photons needed to keep this source ionized turns out to be about $N_{uv} = (3.5 \pm 1.2) \times 10^{48}$ph s^{-1}. Assuming errors of about 10% in both the distance and the radio continuum flux density, we conclude that the exciting star should be an O7V (Martins et al. 2005).

In a rough attempt to identify the star(s) candidate(s) responsible for the ionized gas in the region we performed an optical and infrared photometric study of the point sources in the area (see Fig. 2) based on the astrometric UCAC3 Catalog (Zacharias et al. 2010). Only sources with detection in the optical B and R bands, and in the three near-infrared (NIR)

---

[6]http://third.ucllnl.org/gps/

J,H,K bands extracted from the Two Micron All Sky Survey (2MASS)[7], were considered. We found eight sources inside a circle of size 4′ centered at the central coordinate of the HII region. Their locations are shown in Fig. 2. From the optical and infrared magnitudes we constructed their spectral energy distribution (SED). We fit the available magnitudes (optical B and R bands, the three *JHK* 2MASS bands, and the four *Spitzer*-IRAC bands) using the Kurucz photospheric models (Kurucz 1979) included in the tool developed by Robitaille et al. (2007)[8] to obtain the effective temperature, T_{eff}, of each source. The fitting tool requires the assumption of the visual extinction, A_v, and the distance. We adopt a distance between 3.5 and 4.5 kpc. Regarding the A_v, we derived it for each source from their *(J−H)* and *(H−K)* colors. We assumed the interstellar reddening law of Rieke & Lebofsky (1985) ($A_J /A_V = 0.282$, $A_H /A_V = 0.175$, and $A_K /A_V = 0.112$) and the intrinsic colors *(J−H)$_0$* and *(H−K)$_0$* obtained by Martins & Plez (2006).

Among the eight stars found in the region, only three are compatible with a massive star located at the distance of G46. The effective temperatures of the massive candidates stars obtained from the fitting are shown in Table 1. Stars #6 and #8 have a T_{eff} of about 30000 K and 35000 K, respectively, which agree with the temperatures of O9.5V and O7V stars, respectively (Schaerer & de Koter 1997). The models predict an effective temperature of $\sim$ 26000 K for source #3, suggesting that this star would be of a spectral type later than B0. The fitted SEDs for sources #6 and #8 are shown in Fig. 3. For the remaining sources #1, #2, #4, #5 and #7, the Kurucz's models fail to fit with confidence their optical and NIR magnitudes as a massive star at about 4 kpc. These sources are

---

[7]2MASS is a joint project of the University of Massachusetts and the Infrared Processing and Analysis Center/California Institute of Technology, funded by the National Aeronautics and Space Administration and the National Science Foundation.

[8]http://caravan.astro.wisc.edu/protostars/

probably less massive foreground stars not related with G46. Thus, stars #6 and #8 are the most probable candidates to be the exciting stars of the HII region. Finally, the location of the star #8 with respect to the radio continuum emission (red in Fig. 2), which looks like an incomplete ring, seems to better explain the curved morphology observed in the ionized gas distribution.

3.2. Molecular gas analysis

The HII region G46 is located in projection onto a border of the molecular cloud GRSMC G046.34-00.21 catalogued by Rathborne et al. (2009) with an associated v_{LSR} of 54.3 ± 3.9 km s^{-1}. Roman-Duval et al. (2009) established a kinematical distance of about 4 kpc for this molecular cloud, the same as for the HII region G46, supporting that both objects are linked. Figure 4 (left) displays the ^{13}CO J=1–0 integrated emission distribution in the $40 - 62$ km s^{-1} velocity range. It can be seen that the HII region seems to be evolving on the northeastern edge of the cloud. The molecular gas appears located in projection onto the diffuse emission at 8 μm observed towards the southwest of the open border of G46. It is noteworthy that there is no evidence of related molecular emission towards the east-northeast edge of the HII region, where its associated PAHs emission is thicker and more intense.

The numerous studies of HII regions and their surroundings usually show that the associated PAHs emission is more intense towards the borders of the HII regions with presence of molecular material. In other words, it is expected that an ionized bubble opens in the direction away from the cloud edge because the ionized gas would be less confined and could stream-out into the lower density ISM, forming what is known as a "blister-type" HII region (Israel 1978; Tenorio-Tagle 1979). In the G46 case, however, the ring opens to the southwest, facing the elongated molecular cloud where apparently the density is higher.

A possible explanation can be found from the morphology of the G46 radio continuum emission, which suggests a stalling effect of the ionized gas against the photodissociation region (PDR) towards the northeast (see Fig. 2). This fact suggests that although there is no ^{13}CO J=1–0 detected towards this region, the density of the photodissociated gas is enough to confine the ionized gas. The atypical thickness of the PDR towards this edge could be due to the presence of relatively low density gas which is expected towards the edge of a molecular cloud whereby the far-UV photons would have greater penetration in the material. By the other hand, the non detection of radio continuum emission towards the open border of G46 suggests that the ionized gas escapes from G46 and dilutes in the ISM. The presence of diffuse emission at 8 μm towards the southwest of G46 supports this scenario.

3.2.1.   The pillar-like features

As above mentioned, about 10′ towards the southwest of the H\textsc{ii} region ($\sim$12 pc at the assumed distance of 4 kpc) it can be seen some pillar-like features emitting at 8 μm, which are pointing to the ionizing source of G46 and seem to be embedded in the molecular cloud GRSMC G046.34-00.21. Even though it seems to be a large distance, several pillars were found as far from the ionizing source as those analyzed in this work (e.g in the Vulpecula rift; Billot et al. 2010). What it is really remarkable in this case is that these pillars-like features, resembling heaps and corrugations, are well outside of the H\textsc{ii} region, in contrary as is usually found: bubble-like structures with pillars inside or over their boundaries. Taking into account that the pillars point to the G46 open border, it is suggested that they were produced by UV photons escaped from the H\textsc{ii} region.

By inspecting the ^{13}CO J=1–0 towards the pillar-like features (Fig. 4-right), we find that there are two molecular structures associated with them. The easternmost IR pillar-like

feature has associated molecular gas between 54.0 and 56.5 km s^{-1} (white contours in Fig. 4-right), while the western one is related to a molecular structure ranging between 56.5 and 59.0 km s^{-1} (yellow contours in Fig. 4-right). The different velocity ranges for these molecular structures may either indicate that both features are located at slightly different positions along the line of sight or that they have a somewhat different kinematics. It is remarkable the good agreement between the morphology of the molecular gas and the pillar-like features as seen in IR. Moreover, the molecular structures present a morphology consisting of a dense head with a less dense tail as is usually found and predicted by models and observations towards this kind of structures in the surroundings of H$_{II}$ regions (Pound et al. 2007; Schuller et al. 2006; Pound et al. 2005). However, following the work of Mackey & Lim (2010), the appearance of these structures resembles a previous evolutive stage in the formation of pillars because it can not be appreciated a well-formed tail behind their heads. In what follow we characterize the interaction between the ionization radiation escaping from G46 and the pillar-like features.

In order to study the radiation influence over the tips of the pillar-like features and the possibilities of triggered star formation via radiative driven implosion (RDI, e.g. Bertoldi 1989, Lefloch et al. 1997, Kessel-Deynet & Burkert 2003) we evaluate the pressure balance between the ionized gas stalling at the head of the pillars and the neutral gas of their interiors. Assuming that the ionizing photons came from an O7V-type star located at the center of G46 (see Sect. 3.1), we use the predicted ionizing photon flux for an O7V star from Schaerer & de Koter (1997) and the projected distance between the star and the pillars to roughly estimate the amount of UV photons arriving at the surface of the pillars in $\Phi_{pre} \sim 2 \times 10^8$ cm^{-2} s^{-1}. This value represents an upper limit due to the fact that the projected distance between the star and the pillars is a lower limit to the actual distance between them. Our predicted ionizing photon flux is similar to those measured towards several bright-rimmed clouds (Thompson et al. 2004a,b), which like the pillars, are

molecular clouds sculpted by the radiation leaking from HII regions, and in many cases they have the same large scale morphology as the pillars (Thompson et al. 2004a).

Using the above obtained Φ_{pre} and following Thompson et al. (2004b) we estimate an upper limit for the electron density of about 64 cm^{-3} for the expected ionized boundary layer (IBL) at the tip of both pillar-like structures. This is almost 3 times greater than the critical value of ~ 25 cm^{-3} above which an IBL is able to develop around a cloud (Lefloch & Lazareff 1994). To obtain this value we consider that the pillar heads have a radius of 0.5' and assume an effective thickness of the ionized boundary layer of $\eta = 0.1$. Then, using a typical sound speed of the ionized gas of 11.4 km s^{-1}, we obtain that the pillars tips are supporting an external pressure of P$_{ext}/k \sim 2.1 \times 10^6$ cm^{-3} K. It is important to note that the obtained P$_{ext}$ represents strictly an upper limit because the predicted Φ is an upper limit and due to the used η (see Thompson et al. 2004b).

On the other side, integrating the ^{13}CO J=1–0 emission over the area that contain each pillar head and using the typical LTE formulae to derive the ^{13}CO and H$_2$ column densities by assuming a T$_{ex}$ = 10 K and [H$_2$/^{13}CO] $= 5 \times 10^5$ (see e.g. Yamaguchi et al. 1999), we estimate the mass of each pillar head in about 450 and 300 M$_\odot$ for the eastern and western one, respectively. The area of each pillar head was assumed by taking into account the radius of their tips curvature, this is a circular area with radius of 0.5' for both pillar heads. Thus, assuming spherical shapes, we estimate the molecular densities in about 7.0×10^3 and 4.6×10^3 cm^{-3}, respectively. Then, considering the velocity interval in which each pillar structure extends, we obtain the velocity dispersion $\sigma_v \sim 1.05$ km s^{-1}, which is in agreement with those predicted by models of pillars formation (Gritschneder et al. 2010; Dale et al. 2012). Finally, using the obtained densities and σ_v we derive the internal pressure for each pillar head in P$_{int}/k \sim 1.8 \times 10^6$, and $\sim 1.2 \times 10^6$ cm^{-3} K for the eastern and western one, respectively. As Thompson et al. (2004b) state, these pressure values are

very likely underestimated because the ^{13}CO J=1–0 line underestimates the true density and this molecule may be depleted by selective photodissociation at the boundary of the clouds. Following these authors, the internal pressure is likely underestimated by no more than a factor of 15, thus we conclude that P_{int}/k should be between 2×10^6 and 3×10^7 cm^{-3} K.

In conclusion, we obtain $P_{int} > P_{ext}$, which suggests that the diluted ionization front stalls at the pillar heads, probably until the effects of mass evaporation and increasing recombination within the IBL raises the ionized gas pressure to equilibrium with the interior pressure (Lefloch & Lazareff 1994). This result shows that it is unlikely that a shock is propagating farther into the molecular gas, discarding that the RDI mechanism is on going in the pillars interior.

3.2.2. The molecular gas towards G46 open border

With the purpose of investigating the molecular material towards the open border of G46 we used higher-angular resolution data of several molecular species extracted from the JCMT database acquired towards this region (see the rectangle in Fig. 4-left). Figure 5 shows the integrated emission of the ^{12}CO, ^{13}CO, and C^{18}O J=3–2, while Fig. 6 displays the HCO$^+$ and HCN J=4–3 integrated emission. The ^{12}CO and ^{13}CO J=3–2 emission show clumpy, elongated molecular features, with a high density filament extending towards the southwest of the mapped region. Towards the open border of G46 do not appear any considerable molecular emission, suggesting the presence of a pre-existing region with scarce molecular gas or that the UV-photons have carved the molecular cloud. In any case this can be the path followed by the UV-photons escaped from G46 to reach the farther pillar-like structures.

The C^{18}O J=3–2, HCO$^+$ and HCN J=4–3 emissions are concentrated in a small compact clump related to the infrared dark cloud IRDC 046.424-0.237 (Peretto & Fuller 2009) and to the millimeter continuum source BGPS G046.427-00.237 (see the Bolocam Galactic Plane Survey v2; Ginsburg et al. 2013), suggesting that the emission lines emanate from a deeply embedded clump. Moreover, this structure is associated with the cold high-mass clump G46.43-0.24 (Wienen et al. 2012) in which the (1,1) and (2,2) ammonia lines were detected at $v_{LSR} \sim 52.3$ and 52.9 km s^{-1}, respectively. The detection of these molecular species, mainly the HCN J=4–3 line that its critical density can be between some 10^6 and 10^8 cm^{-3} (Takakuwa et al. 2007; Greve et al. 2009), indicates the presence of very high density gas. Taking into account that this clump is a potential site of star formation, in what follows we analyze it.

The line parameters of the observed molecular transitions towards the center of the clump are given in Table 2 as derived from Gaussian fits from the spectra shown in Fig. 7. The ^{12}CO J=3–2 was fitted using three Gaussians, while the parameters of the others lines were obtained from single-components Gaussian fits which coincide in velocity with the main ^{12}CO component. The different velocity components observed in the ^{12}CO spectrum are present almost in the whole region. Thus, we conclude that they correspond to different molecular components seen along the line of sight, reflecting the clumpiness in the region.

In order to have a rough estimate of the molecular clump mass we assume local thermodynamic equilibrium (LTE). We calculate the excitation temperature from

$$T_{ex}(3 \rightarrow 2) = \frac{16.59\text{K}}{\ln[1 + 16.59\text{K}/(T_{\max}(^{12}\text{CO}) + 0.036\text{K})]} \tag{1}$$

where $T_{\max}(^{12}\text{CO})$ is the ^{12}CO peak temperature towards the clump center at ~ 52 km s^{-1}, obtaining T$_{ex} \sim 18$ K. We derive the ^{13}CO and C^{18}O optical depths τ_{13} and τ_{18} from (e.g. Buckle et al. 2010):

$$\frac{^{13}\text{T}_{mb}}{^{18}\text{T}_{mb}} = \frac{1 - exp(-\tau_{13})}{1 - exp(-\tau_{13}/X)}, \tag{2}$$

where $^{13}T_{mb}$ and $^{18}T_{mb}$ are the peak temperatures of the ^{13}CO and C^{18}O J=3–2 line at the center of the region, and $X = 8.4$ is the assumed isotope abundance ratio [^{13}CO/C^{18}O] (Frerking et al. 1982; Wilson 1999), obtaining $\tau_{13} \sim 3.5$ and $\tau_{18} \sim 0.4$, which indicate that the C^{18}O J=3–2 line appears moderately optically thin. Thus, we estimate its column density from:

$$N(C^{18}O) = 8.26 \times 10^{13} \; e^{\frac{15.81}{T_{ex}}} \frac{T_{ex} + 0.88}{1 - e^{\frac{-15.81}{T_{ex}}}} \frac{1}{J(T_{ex}) - J(T_{BG})} \int T_{mb} \; dv \tag{3}$$

with

$$J(T) = \frac{h\nu/k}{exp(\frac{h\nu}{kT}) - 1}. \tag{4}$$

To obtain the molecular hydrogen column density N(H$_2$) we assume an abundance ratio of [H$_2$/C^{18}O] $= 5.88 \times 10^6$ (Frerking et al. 1982; Wilson 1999). Finally the mass was derived from:

$$M = \mu \; m_H \sum_i \left[D^2 \; \Omega_i \; N_i(H_2) \right], \tag{5}$$

where Ω is the solid angle subtended by the beam size, m_H is the hydrogen mass, μ, the mean molecular weight, is assumed to be 2.8 by taking into account a relative helium abundance of 25 %, and D is the distance. Summation was performed over all beam positions on the molecular structure observed in C^{18}O displayed in contours in Fig. 5. The obtained mass is about 375 M$_\odot$. Assuming an ellipsoidal volume with semi-axis of 45″, 20″, and 20″ we derive a density of n $\sim 1.5 \times 10^4$ cm^{-3}. The density should be higher in the innermost region of the clump where the HCN J=4–3 line emanates, showing a density gradient. Using the deconvolved radius of about 0.5 pc calculated from:

$$R_{clump} = \sqrt{\frac{S - \text{beam area}}{\pi}} \tag{6}$$

where S is the area inside the clump, we appreciate that the above obtained mass value is slightly over the mass–size threshold for massive star formation in IRDCs presented in Kauffmann & Pillai (2010), suggesting that massive YSOs can be formed within this clump.

Using the derived HCO^+ and HCN J=4–3 parameters listed in Table 2 we performed a non-LTE study of these molecular species with the code RADEX, which uses the mean escape probability approximation for the radiative transfer equation (van der Tak et al. 2007). Using the measured Δv we ran the code to fit T_{mb} and estimate the column densities. Taking into account that Wienen et al. (2012) measured from the ammonia lines a kinetic temperature of $T_k \sim 16$ K towards this clump, we fix this parameter in 20 K and assume densities between 10^5 and 10^7 cm^{-3} to obtain the values presented in Table 3. From the obtained column densities we observe abundance HCN/HCO^+ ratios of about 4.4, 3.8, and 1.2 for $n_{H_2} = 10^5$, 10^6, and 10^7 cm^{-3}, respectively. In all cases we obtain a $N(HCN)/N(HCO^+)$ ratio larger than unity as found towards several clumps in the IRDC G48.66-0.22 (Pitann et al. 2013) and the active star-forming region W49A (Roberts et al. 2011). As these authors point out, the steady-state chemical models for molecular species in gas-phase predict HCN > HCO^+ only for $T_k < 25$ K, with a density of $n_{H_2} = 10^6$ cm^{-3}, which is consistent with our results.

3.3. Star formation around G46

Finally, given that the scenario is very favorable to initiate the formation of new generations of stars, we analyze in this section the existence and properties of young stellar objects in all the investigated area.

3.3.1. Identification of YSOs

Young stellar objects (YSOs) always show an excess in the infrared emission. The level of excess in the infrared can be effectively used for discriminating YSOs from field stars and distinguishing different evolutionary stages. At a considerably early evolutionary stage,

protostars are mostly embedded in dust envelopes, they exhibit large excess of infrared emission and an infrared spectral index $\alpha_{\rm IR} > -0.3$ indicative of flat or ascending spectral energy distribution (SED) at wavelength longward of 2 μm (Lada 1987; Greene et al. 1994). For pre-main sequence (PMS) stars which possess optically thick disks, the SEDs tend to descend and the infrared spectral indices are in the range $-1.6 < \alpha_{\rm IR} < -0.3$. Finally "transition disk" sources are more evolved YSOs, where the inner part of the disks have been cleared by photoevaporation of the central stars or by planet forming processes. For such YSOs it is expected to detect IR excess at wavelengths longer than 16 μm (Strom et al. 1989). These properties of YSOs make photometric observations in the near- to mid-infrared plausible to discriminate them from field stars. Different color-based source identification and classification schemes have been developed and verified in the practice. In this section, we identify potential YSOs following the scheme proposed by Gutermuth et al. (2009). The resulting YSOs are classified into Class I (protostars, including Class 0, Class I, and "flat spectrum" sources), Class II, and "transition disk" sources.

There are several kinds of contaminants that could be misidentified as YSOs in our original sample. Extragalactic contaminations could stem from star-forming galaxies and broad-line active galactic nuclei (AGN), which show PAH feature emission yielding very red 5.8 and 8.0 μm colors (Stern et al. 2005; Gutermuth et al. 2008). In our own Galaxy, unresolved knots of shock emission and resolved PAH emission are often detected in the IRAC bands, yielding additional contaminations. Following the techniques presented in Gutermuth et al. (2009) we exclude contaminants, and then identify and categorize potential YSOs as described as follows.

In the first phase, only sources with valid detections in all four IRAC bands have been considered. Any source fulfilling color criteria of $[3.6] - [4.5] > 0.7$ and $[4.5] - [5.8] > 0.7$ is regarded as a Class I YSO. In the remaining pool, Class II sources have been picked out

based on the constraints of i) $[3.6] - [4.5] - \sigma_1 > 0.15$, ii) $[3.6] - [5.8] - \sigma_2 > 0.35$, iii) $[4.5] - [8.0] - \sigma_3 > 0.5$, and iv) $[3.6] - [5.8] + \sigma_2 \leq \frac{0.14}{0.04} \times (([4.5] - [8.0] - \sigma_3) - 0.5) + 0.5$. Here, $\sigma_1 = \sigma([3.6] - [4.5])$, $\sigma_2 = \sigma([3.6] - [5.8])$, and $\sigma_3 = \sigma([4.5] - [8.0])$ are combined errors, added in quadrature.

In the second phase, sources with 24 μm data in the remaining pool are reexamined. Sources with colors of $[5.8] - [24] > 2.5$ or $[4.5] - [24] > 2.5$ are classified to be "transition disks". With the potential contaminants and YSOs identified above excluded, there still remain some sources with bright 24 μm emission. For sources lacking valid photometric data in one or more of the IRAC bands, they are picked out as additional Class I type YSOs once fulfilling $[24] > 7$ and $[X] - [24] > 4.5$ mag, where $[X]$ is the longest wavelength IRAC detection that we have.

The classification scheme of Gutermuth et al. (2009) includes three phases, using 2MASS data to identify more YSOs in addition to the aforementioned methods. However, in our case as G46 is much farther than the sources in Gutermuth et al. (2009), 2MASS photometry would be severely affected by foreground interstellar extinction and the use of these near-IR data to identify YSOs would induce heavy contamination from foreground field stars. Thus, we do not use the near-IR bands in our YSOs search.

The above identification procedures have resulted in 106 YSOs. And they are classified into 22 Class I, 60 Class II, and 24 "transition disks" objects. A summary of the results is given in Table 4. We note that the color based classification scheme would lead to misidentification. A Class II YSO viewed at high inclination would show features resembling that of a Class I source. An edge-on Class I YSO can have similar infrared color of a Class 0 source. Thus, all Class I, II, and "transition disk" sources identified in this paper are YSO candidates. The distribution of these YSO candidates on distinct color-color spaces are presented in Figs. 8 and 9. It is important to note that we also use the point

sources extracted from Gutermuth & Heyer (2015) to identify YSO candidates and reached identical results.

3.3.2.   Active Star Formation in GRSMC G046.34-00.21

Figure 10(a) shows the large scale spatial distribution of the 106 YSOs identified in the region. Among the 82 Class I and Class II YSOs more than 40 (about 50 percent) are located in projection onto the molecular cloud GRSMC G046.34-00.21 (see Fig. 4) which fills only the 20 percent of the whole survey field. Such a concentration of YSOs is suggestive of active star formation taking place in the cloud. By the other hand, from the 24 "transition disk" found in the whole field, no one is detected in association with the molecular gas, indicating the relatively young nature of the YSOs embedded in this cloud. Interestingly all YSOs associated with the molecular cloud are placed in projection between the open border of G46 and the head of the pillars. Moreover, there are not young sources in the farthest part of the cloud behind the heads of these pillars (see Fig. 10(b)).

From Figure 10(a) it can be appreciated only two concentrations of young objects over the whole field, one centered at 19^h16^m30ß, $+11°51'00''$ (J2000), consisting of 15 Class II type sources and the other one centered at 19^h17^m00ß, $+11°47'00''$ (J2000) mostly composed by Class I type YSOs (9 sources), which are located just ahead the pillars-like features. A closeup view of the pillar-like features region is shown in Figure 10(b). There is a point source revealed at 24 μm which is too faint at IRAC bands and not listed in the GLIMPSE catalog. We have marked this 24 μm point source using a red circle in Figure 10(b). Weak at short wavelengths, this point source would be younger than other ones and could be a Class 0 candidate.

The fact that the Class II concentration is located closer to the open border of G46

than the Class I group strongly suggests an age gradient in the YSOs distribution. By the other hand, the absence of young sources inside and behind the pillar-like structures could show that the Hɪɪ region influence has not reached the molecular material behind the pillars, which is in agreement with the result of Section 3.2.1. We suggest a scenario where the propagation of ionization radiation escaping from the Hɪɪ region has triggered the star formation observed in the molecular cloud through RDI mechanism and then has stalled at the surface of the pillars heads. We can not discard that a growing density of the IBL reaches equilibrium with that of the cloud and thus, the shock front will continue their propagation into the cloud (Thompson et al. 2004a).

Additionally, in the region surveyed with the JCMT (see yellow rectangle in Fig. 4) there are 5 YSO candidates. One of them, a Class I source, lies exactly at the center of the dense molecular clump mapped with the HCO$^+$ and HCN J=4–3 (see Fig. 6), which is in agreement with the molecular gas conditions studied in Sec. 3.2.2.

4.   Conclusions

We have analyzed the Hɪɪ region G46.5-0.2, its molecular environment and the young stellar objects placed in a wide region around it, searching for evidence of their physical connection and the possibility of induced star formation. We found a rich combination of mutual influences, underscoring the important role of Hɪɪ regions in favoring the formation of new stars not only on their immediate vicinity but also farther than a distance equivalent to its own radius.

We characterized that the Hɪɪ region, located at about 4 kpc and with a radius of ~ 4.6 pc, is probably excited by an O7V star. Its shape resembles a horse-shoe, with the bright, thick border towards the east-northeast and the open portion towards the southwest side.

When mapping the distribution of the molecular gas associated with G46 we found that the Hɪɪ region is located close to the edge of the GRSMC G046.34-00.21 molecular cloud and, curiously, G46 instead of opening in the direction of lower ambient density it does exactly in the opposite direction, towards the cloud. Filamentary structure in the molecular cloud is observed, particularly in the ^{12}CO J=3–2 and ^{13}CO J=3–2 maps. Towards the open border of G46 do not appear any considerable molecular emission, suggesting the presence of a pre-existing region with scarce molecular gas or that the UV-photons have carved the molecular cloud. Besides, close to the end of the observed filamentary structures in the cloud, the infrared images reveal the existence of pillar-like structures pointing towards the Hɪɪ region open border, which are associated with some narrow molecular filaments characterized using the ^{13}CO J=1–0 line. From a pressure balance study we found that the internal pressure of the neutral gas in the pillar-like features heads are larger than the external pressure due to the ionized gas stalling at their tips, discarding that the RDI mechanism is on going. In addition, we analyzed a compact molecular clump located over the south border of G46, obtaining a mass of ~ 375 M$_\odot$ and a density of about 10^4 cm^{-3}, with a higher density towards its center, where the HCN J=4–3 line is detected.

Taking into account that the expansion of the Hɪɪ region itself, and the injection of extra energy into the molecular cloud can drive turbulence and trigger star formation we searched for candidates of YSOs and classified them according to their evolutionary stage. We identified two main concentrations of young objects over the whole region, one, closer to the G46 open border consisting of Class II type sources, and other one mostly composed by Class I type YSOs located just ahead the pillars-like features strongly suggesting an age gradient in the YSOs distribution.

REFERENCES

Anderson, L. D. & Bania, T. M. 2009, ApJ, 690, 706

Benjamin, R. A., Churchwell, E., Babler, B. L., et al. 2003, PASP, 115, 953

Bertoldi, F. 1989, ApJ, 346, 735

Billot, N., Noriega-Crespo, A., Carey, S., et al. 2010, ApJ, 712, 797

Bisbas, T. G., Wünsch, R., Whitworth, A. P., Hubber, D. A., & Walch, S. 2011, ApJ, 736, 142

Buckle, J. V., Hills, R. E., Smith, H., et al. 2009, MNRAS, 399, 1026

Buckle, J. V., Curtis, E. I., Roberts, J. F., & et al. 2010, MNRAS, 401, 204

Carey, S. J., Noriega-Crespo, A., Mizuno, D. R., et al. 2009, PASP, 121, 76

Chaisson, E. J. 1976, in Frontiers of Astrophysics, ed. E. H. Avrett, 259–351

Dale, J. E., Ercolano, B., & Bonnell, I. A. 2012, MNRAS, 424, 377

Deharveng, L., Lefloch, B., Kurtz, S., et al. 2008, A&A, 482, 585

Dirienzo, W. J., Indebetouw, R., Brogan, C., et al. 2012, AJ, 144, 173

Elmegreen, B. G., Kimura, T., & Tosa, M. 1995, ApJ, 451, 675

Fazio, G. G., Hora, J. L., Allen, L. E., et al. 2004, ApJS, 154, 10

Frerking, M. A., Langer, W. D., & Wilson, R. W. 1982, ApJ, 262, 590

Ginsburg, A., Glenn, J., Rosolowsky, E., et al. 2013, ApJS, 208, 14

Greene, T. P., Wilking, B. A., Andre, P., Young, E. T., & Lada, C. J. 1994, ApJ, 434, 614

Greve, T. R., Papadopoulos, P. P., Gao, Y., & Radford, S. J. E. 2009, ApJ, 692, 1432

Gritschneder, M., Burkert, A., Naab, T., & Walch, S. 2010, ApJ, 723, 971

Gutermuth, R. A., & Heyer, M. 2015, AJ, 149, 64

Gutermuth, R. A., Megeath, S. T., Myers, P. C., et al. 2009, ApJS, 184, 18

Gutermuth, R. A., Myers, P. C., Megeath, S. T., et al. 2008, ApJ, 674, 336

Israel, F. P. 1978, A&A, 70, 769

Jackson, J. M., Rathborne, J. M., Shah, R. Y., et al. 2006, ApJS, 163, 145

Kauffmann, J., & Pillai, T. 2010, ApJ, 723, L7

Kessel-Deynet, O. & Burkert, A. 2003, MNRAS, 338, 545

Kuchar, T. A. & Bania, T. M. 1994, ApJ, 436, 117

Kurucz, R. L. 1979, ApJS, 40, 1

Lada, C. J. 1987, in IAU Symposium, Vol. 115, Star Forming Regions, ed. M. Peimbert & J. Jugaku, 1–17

Lefloch, B., & Lazareff, B. 1994, A&A, 289, 559

Lefloch, B., Lazareff, B., & Castets, A. 1997, A&A, 324, 249

Lockman, F. J. 1989, ApJS, 71, 469

Martins, F. & Plez, B. 2006, A&A, 457, 637

Martins, F., Schaerer, D., & Hillier, D. J. 2005, A&A, 436, 1049

Mackey, J., & Lim, A. J. 2010, MNRAS, 403, 714

Maíz-Apellániz, J., Walborn, N. R., Galué, H. Á., & Wei, L. H. 2004, ApJS, 151, 103

Maíz Apellániz, J., Sota, A., Morrell, N. I., et al. 2013, Massive Stars: From alpha to Omega, 198

Ortega, M. E., Paron, S., Giacani, E., Rubio, M., & Dubner, G. 2013, A&A, 556, A105

Panagia, N. 1973, AJ, 78, 929

Paron, S., Petriella, A., & Ortega, M. E. 2011, A&A, 525, A132

Peretto, N., & Fuller, G. A. 2009, A&A, 505, 405

Pitann, J., Linz, H., Ragan, S., et al. 2013, ApJ, 766, 68

Pound, M. W., Kane, J. O., Remington, B. A., et al. 2005, Ap&SS, 298, 177

Pound, M. W., Kane, J. O., Ryutov, D. D., Remington, B. A., & Mizuta, A. 2007, Ap&SS, 307, 187

Quireza, C., Rood, R. T., Balser, D. S., & Bania, T. M. 2006, ApJS, 165, 338

Rathborne, J. M., Johnson, A. M., Jackson, J. M., Shah, R. Y., & Simon, R. 2009, ApJS, 182, 131

Reed, B. C. 2003, AJ, 125, 2531

Rieke, G. H. & Lebofsky, M. J. 1985, ApJ, 288, 618

Rieke, G. H., Young, E. T., Engelbracht, C. W., et al. 2004, ApJS, 154, 25

Roberts, H., van der Tak, F. F. S., Fuller, G. A., Plume, R., & Bayet, E. 2011, A&A, 525, A107

Robitaille, T. P., Whitney, B. A., Indebetouw, R., & Wood, K. 2007, ApJS, 169, 328

Roman-Duval, J., Jackson, J. M., Heyer, M., et al. 2009, ApJ, 699, 1153

Schaerer, D. & de Koter, A. 1997, A&A, 322, 598

Schuller, F., Leurini, S., Hieret, C., et al. 2006, A&A, 454, L87

Skrutskie, M. F., Cutri, R. M., Stiening, R., et al. 2006, AJ, 131, 1163

Stern, D., Eisenhardt, P., Gorjian, V., et al. 2005, ApJ, 631, 163

Stetson, P. B. 1987, PASP, 99, 191

Strom, K. M., Strom, S. E., Edwards, S., Cabrit, S., & Skrutskie, M. F. 1989, AJ, 97, 1451

Takakuwa, S., Ohashi, N., Bourke, T. L., et al. 2007, ApJ, 662, 431

Tenorio-Tagle, G. 1979, A&A, 71, 59

Thompson, M. A., White, G. J., Morgan, L. K., et al. 2004, A&A, 414, 1017

Thompson, M. A., Urquhart, J. S., & White, G. J. 2004, A&A, 415, 627

Tremblin, P., Minier, V., Schneider, N., et al. 2013, A&A, 560, A19

van der Tak, F. F. S., Black, J. H., Schöier, F. L., Jansen, D. J., & van Dishoeck, E. F. 2007, A&A, 468, 627

White, G. J., Nelson, R. P., Holland, W. S., et al. 1999, A&A, 342, 233

Werner, M. W., Uchida, K. I., Sellgren, K., et al. 2004, ApJS, 154, 309

Wienen, M., Wyrowski, F., Schuller, F., et al. 2012, A&A, 544, A146

Wilson, T. L. 1999, Reports on Progress in Physics, 62, 143

Yamaguchi, R., Saito, H., Mizuno, N., et al. 1999, PASJ, 51, 791

Zacharias, N., Finch, C., Girard, T., et al. 2010, AJ, 139, 2184

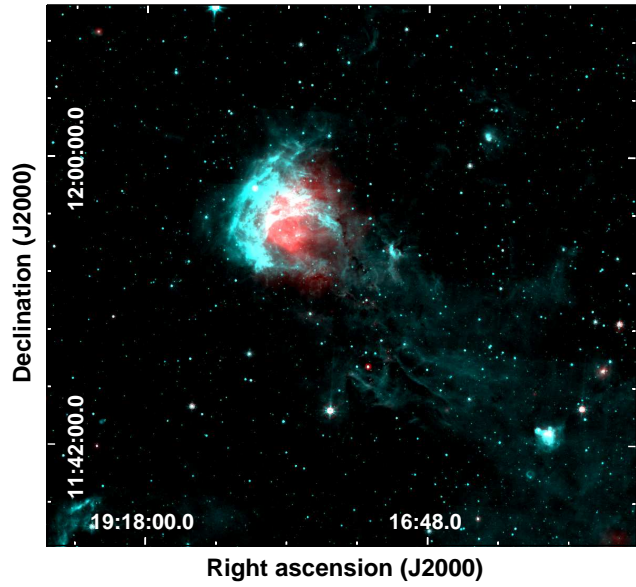Zavagno, A., Anderson, L. D., Russeil, D., et al. 2010, A&A, 518, L101

This manuscript was prepared with the AAS LATEX macros v5.2.

Fig. 1.— Two-color composite image of a large area towards the Hii region G46. In cyan the *Spitzer*-IRAC 8 μm emission, and in red the *Spitzer*-MIPSGAL emission at 24 μm .
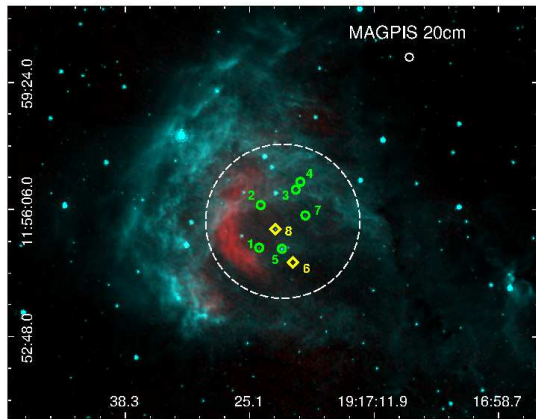

Fig. 2.— Two-color composite image (8 μm = cyan and 20 cm = red). The symbols represent the only eight point sources with *JHK* near-infrared and RB optical bands measurements found in the region (dashed circle). The diamonds (sources #6 and #8) indicate the location of the most likely candidates to be the exciting stars of G46. The beam of the 20 cm emission from MAGPIS is included in the top right corner.
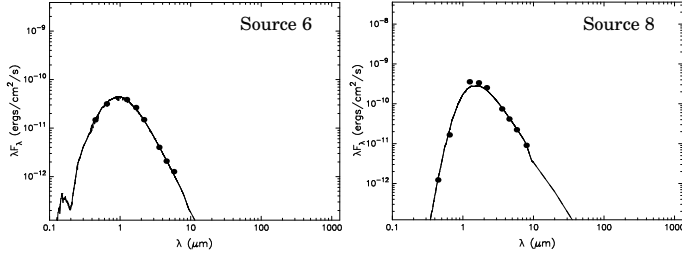
Fig. 3.— Fitting of the spectral energy distribution for sources #6 and #8. The black curves correspond to the best photospheric model of Kurucz (1979). The dots represent the data used for the fitting.
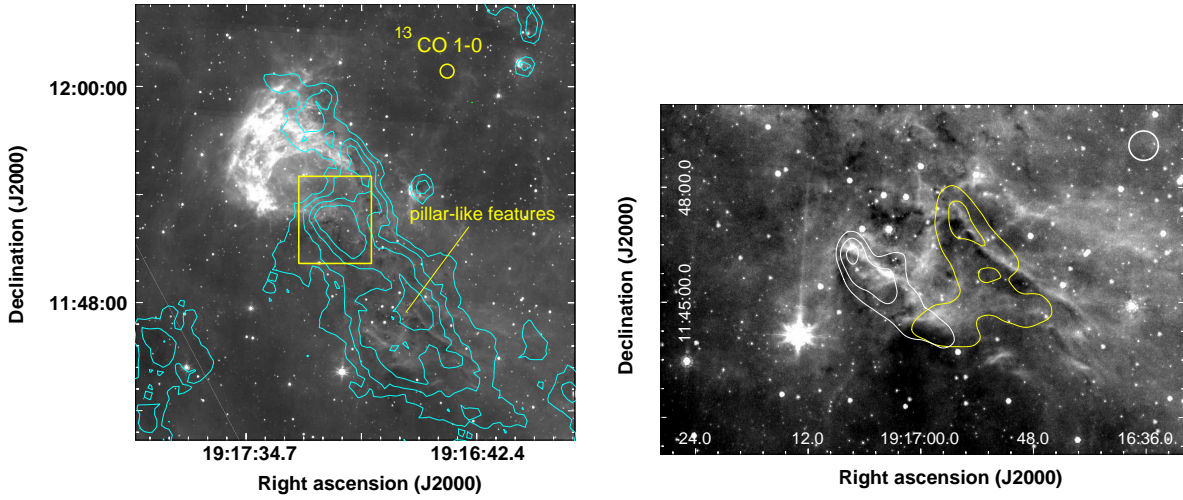

Fig. 4.— Left: *Spitzer*-IRAC 8 μm emission with contours of the ^{13}CO J=1–0 emission integrated between 40 and 62 km s^{-1}, with levels of 10, 15, 20, and 25 K km s^{-1}. The yellow circle is the beam of the observations. The rms noise is about 1 K km s^{-1}. The rectangle represents the region studied with the JCMT data. Right: Integrated ^{13}CO J=1–0 from the GRS towards the pillar-like features observed in 8 μm. The white contours represent the ^{13}CO emission integrated between 54.0 and 56.5 km s^{-1} with levels of 4.5, 5.0, and 5.5 K km s^{-1}, while the yellow ones represent the integration between 56.5 and 59.0 km s^{-1} with levels of 4 and 5 K km s^{-1}. The beam of the molecular data is shown in the top-right corner.
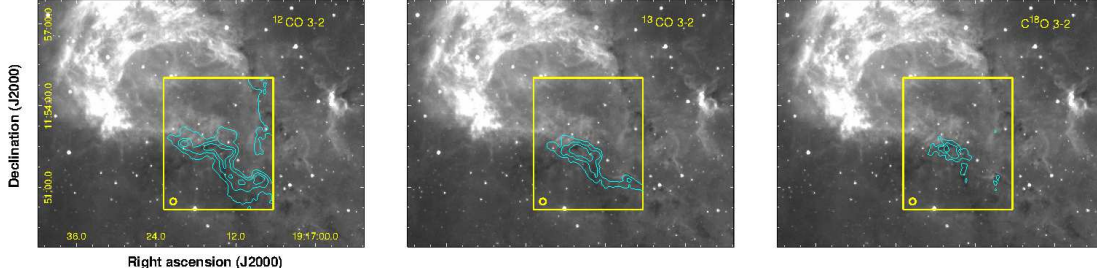
Fig. 5.— ^{12}CO, ^{13}CO, and C^{18}O J=3–2 emission integrated between 40 and 60 km s^{-1} displayed in contours over the *Spitzer*-IRAC 8 μm emission. The contours levels are 45, 58, and 72 K km s^{-1}; 13, 20, and 27 K km s^{-1}; and 3.3, 5.0, and 6.7 K km s^{-1}, for the ^{12}CO, ^{13}CO, and C^{18}O, respectively. The rms noises are about 2.5, 0.8, and 0.5 K km s^{-1}, respectively. The beam of the observations is shown at the bottom left corner of the surveyed region.
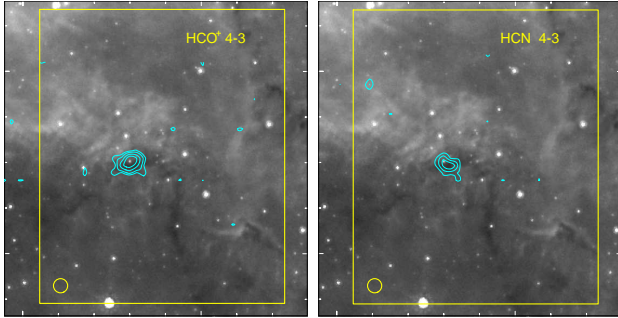

Fig. 6.— *Spitzer*-IRAC 8 μm emission with contours of the J=4–3 transition of the HCO^{+} (left) and HCN (right) integrated between 40 and 65 km s^{-1}. The contours levels are 2.3, 3.3, 5.0, and 8.3 K km s^{-1} for the HCO^{+}, and 1.2, 2.0, and 2.8 K km s^{-1} for the HCN. The rms noise is about 0.3 K km s^{-1} for both emissions. The yellow rectangle represents the same area as shown in previous figures.
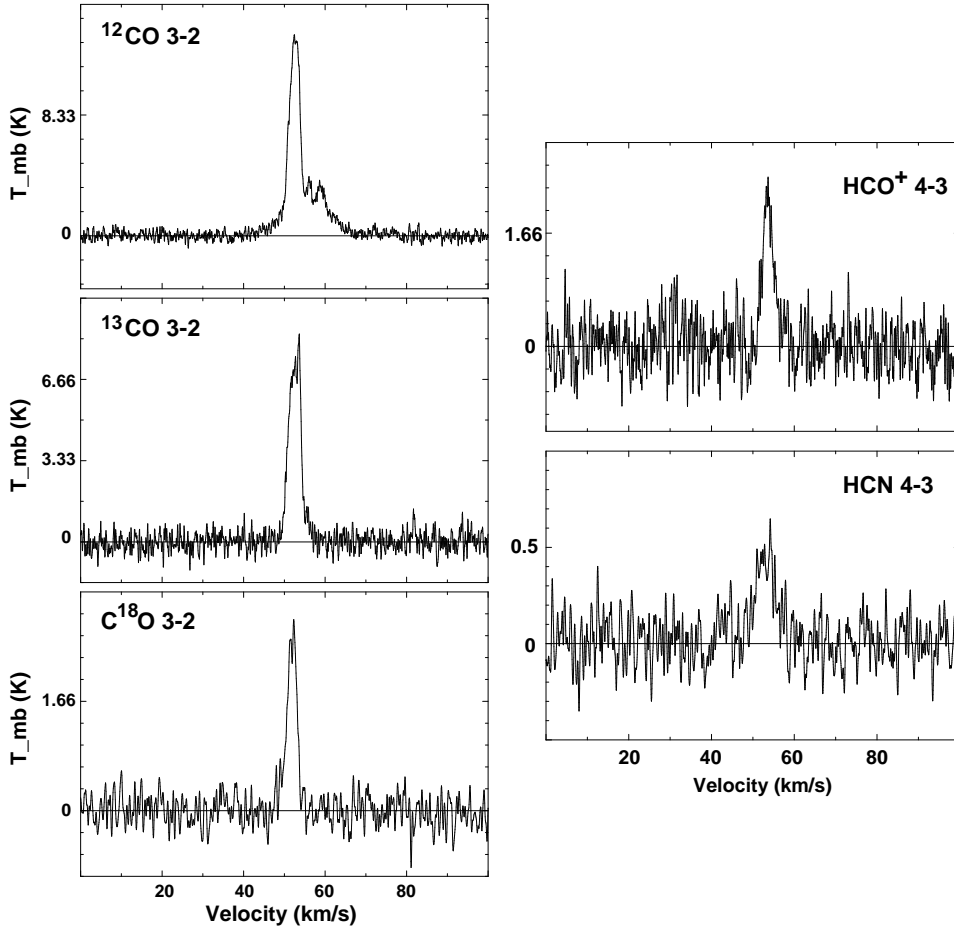
Fig. 7.— Left: CO isotopes spectra. The rms noises of each spectrum are: 250, 400, and 200 mK, respectively. Right: HCO$^+$ and HCN spectra. The rms noises are 33 and 116 mK, respectively. All spectra were obtained towards the center of the dense molecular clump related to the IRDC 046.424-0.237 and to the millimeter continuum source BGPS G046.427-00.237.
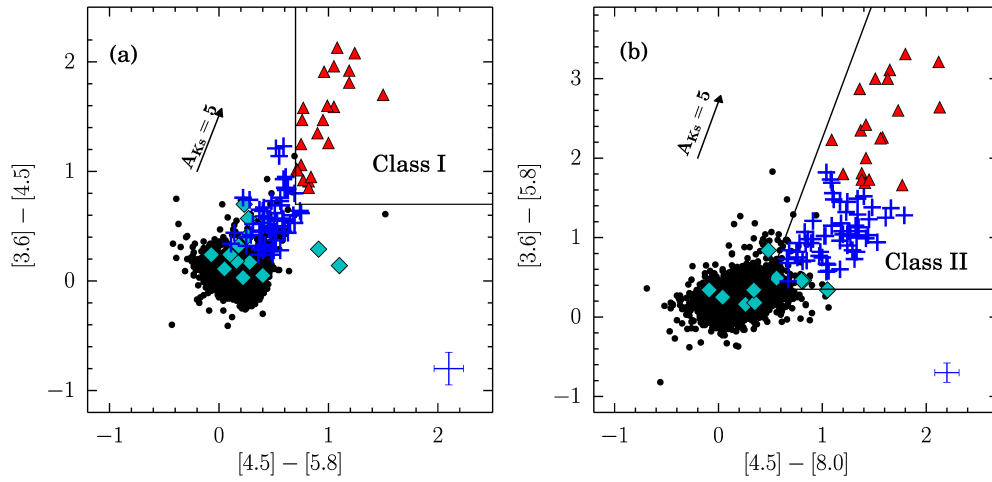
Fig. 8.— IRAC color-color diagrams. Class I, Class II, and "transition disk" YSOs are marked using red triangles, blue plus symbols, and cyan diamonds, respectively. Mean errors of colors are presented in the bottom right corner of each panel. The definition of loci are adopted from Gutermuth et al. (2009).
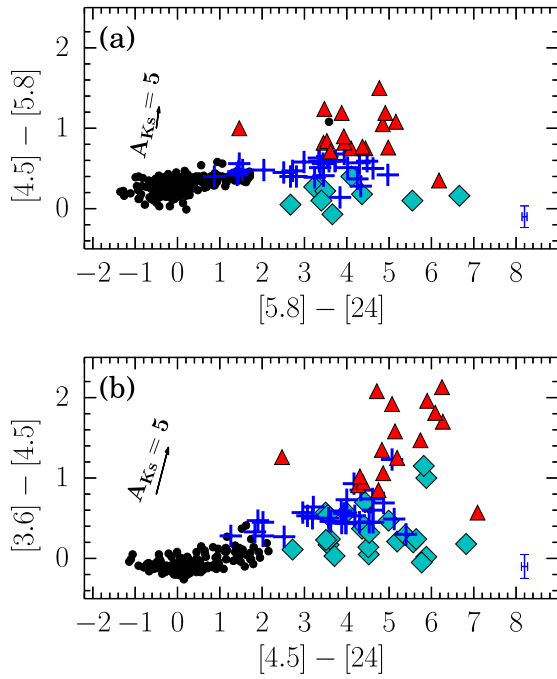
Fig. 9.— IRAC-MIPS color-color diagrams. Class I, Class II, and "transition disk" YSOs are marked using red triangles, blue plus symbols, and cyan diamonds, respectively. Mean errors of colors are presented in the bottom right corner of each panel.
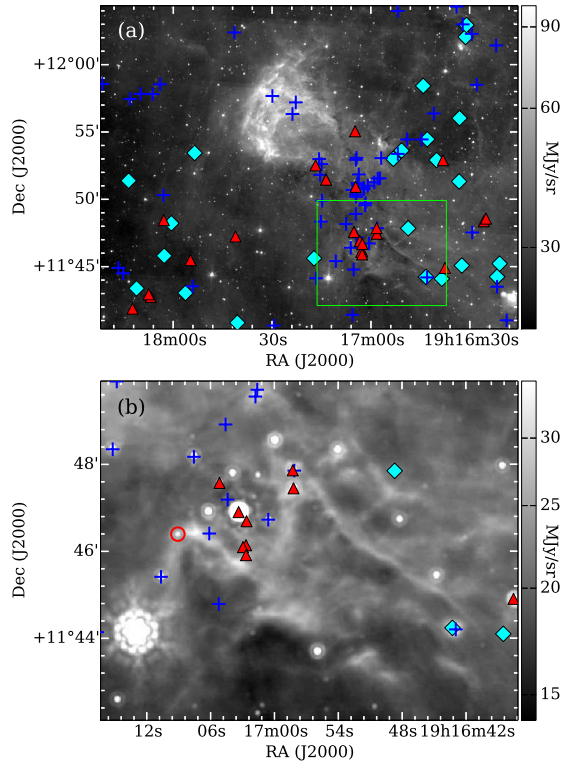
Fig. 10.— (a) Distribution of YSOs. Class I, Class II, and "Transition Disk" YSOs are marked using red triangles, blue plus symbols, and cyan diamonds, respectively. The grayscale shows emission at 8.0 μm. (b) A closeup view of the pillar-like features region. The background presents emission at 24 μm.

Table 1: Exciting star(s) candidate(s) for G46.

#	2MASS Designation	J	H	K	B	R	A_v[mag]	T_{eff}[K]	$\chi^2_{\mathrm{perpoint}}$	Spectral type
3	19172025+1156369	12.508	12.130	11.942	16.80	14.70	4-5	∼26000	1.08	later than B0
6	19172053+1154438	12.498	12.108	11.9815	15.70	14.10	3.5-4.5	∼30000	1.28	∼O9.5V
8	19172239+1155353	10.094	9.353	8.914	18.40	14.80	4-5	∼35000	1.16	∼[O7-O7.5]V

Table 2: Line parameters for the molecular lines towards the center of the southern molecular clump.

Molecular line	T_{mb} peak (K)	v_{LSR} (km s^{-1})	Δv (FWHM) (km s^{-1})
^{12}CO (3–2)	13.90±0.80	52.50±0.05	2.95±0.15
	1.93±0.33	56.10±0.15	0.95±0.25
	2.92±0.25	58.70±0.30	6.10±0.80
^{13}CO (3–2)	7.83±0.25	52.60±0.01	3.47±0.15
C^{18}O (3–2)	2.75±0.33	51.80±0.15	2.80±0.40
HCO$^+$ (4–3)	2.16±0.15	53.70±0.04	3.15±0.10
HCN (4–3)	0.45±0.12	53.10±0.40	5.50±1.00

Table 3: Radex results from the HCO$^+$ and HCN J=4–3 lines using T_k = 20 K and the indicated n_{H_2}.

input n_{H_2} (cm^{-3})	N(HCO$^+$) (cm^{-2})	$\tau_{\mathrm{HCO^+}}$	N(HCN) (cm^{-2})	τ_{HCN}	$X_{\mathrm{HCN/HCO^+}}$
10^5	1.9 ×10^{14}	7.50	8.4 ×10^{14}	4.50	4.42
10^6	1.7 ×10^{13}	0.70	6.5 ×10^{13}	0.37	3.82
10^7	5.4 ×10^{12}	0.14	6.8 ×10^{12}	0.09	1.25

Table 4: Source Counts in the YSO Search

Sources	G46 Field
In GLIMPSE Catalog	19210
Valid in all Four IRAC Bands[a]	4491
With 24 μm data	338
Rejected Contaminants	883
Class I Type	22
Class II Type	60
Transition Disks	24
Total YSO Candidates	106

[a]Sources with photometric uncertainties no larger than 0.2 mag in all four IRAC bands.